LA-UR-11-10487
Approved for public release; distribution is unlimited.

Title: MCNPX-CINDER'90 Simulation of Photonuclear Mo-99 Production Experiments

Author(s): Kelsey, Charles T. IV
Chemerizov, Sergey D.
Dale, Gregory E.
Harvey, James T.
Tkac, Peter
Vandegrift, George R III

Intended for: Tenth International Topical Meeting on Nuclear Applications of Accelerators, 2011-04-03/2011-04-07 (Knoxville, Tennessee, United States)

MCNPX-CINDER'90 SIMULATION OF PHOTONUCLEAR MO-99 PRODUCTION EXPERIMENTS

C.T. Kelsey IV[1], G.E. Dale[1], S.D. Chemerisov[2], J.T. Harvey[3], P. Tkac[2], and G.F. Vandegrift III[2]

[1]*Los Alamos National Laboratory, P.O. Box 1663, Los Alamos, NM 87545, ckelsey@lanl.gov*
[2]*Argonne National Laboratory, 9700 S. Cass Avenue, Argonne, IL 60439, chemerisov@anl.gov*
[3]*NorthStar Medical Radioisotopes, LLC, 706 Williamson St. Suite 2, Madison, WI 53703, jharvey@northstarnm.com*

The MCNPX and CINDER'90 codes were used to support design of experiments investigating Mo-99 production with a 20-MeV electron beam. Bremsstrahlung photons produced by the electron beam interacting with the target drive the desired Mo-100(γ,n)Mo-99 reaction, as well as many undesired reactions important to accurate prediction of radiation hazards. MCNPX is a radiation transport code and CINDER'90 is a transmutation code. They are routinely used together for accelerator activation calculations. Low energy neutron fluxes and production rates for non-neutron and high energy neutron induced reactions computed using MCNPX are inputs to CINDER'90. CINDER'90 presently has only a neutron reaction cross section library up to 25 MeV and normally the other reaction rates come from MCNPX physics models. For this work MCNPX photon flux tallies modified by energy response functions prepared from evaluated photonuclear cross section data were used to tally the reaction rates for CINDER'90 input. The cross section evaluations do not provide isomer to ground state yield ratios so a spin based approximation was used. Post irradiation dose rates were calculated using MCNPX with CINDER'90 produced decay photon spectra. The sensitivity of radionuclide activities and dose rates to beam parameters including energy, position, and profile, as well as underlying isomer assumptions, was investigated. Three experimental production targets were irradiated, two natural Mo and one Mo-100 enriched. Natural Mo foils upstream of the targets were used to analyze beam position and profile by exposing Gafchromic film to the foils after each irradiation. Activation and dose rate calculations were rerun after the experiments using measured beam parameters for comparison with measured Mo-99 activities and dose rates.

I. INTRODUCTION

The daughter product of Mo-99, Tc-99m, is the most commonly used radioisotope for nuclear medicine. This radioisotope is used in approximately two-thirds of all nuclear medicine imaging procedures, amounting to approximately 50,000 diagnostic nuclear medicine procedures performed every day in the United States (US). Until recently, the entire US supply of Mo-99 for nuclear medicine has been produced in two aging foreign reactors using highly enriched uranium (HEU) targets. Recent maintenance and repair shutdowns of these reactors have significantly disrupted the supply of Mo-99 in the US and much of the rest of the world. Additionally, a forecasted supply shortage of HEU for targets in the European production reactors is anticipated to cause significant future supply disruptions as well.

The National Nuclear Security Administration's (NNSA's) Global Threat Reduction Initiative (GTRI, NA 21), in partnership with commercial entities and the US national laboratories, is working to address the need for a reliable domestic supply of Mo-99 for nuclear medicine while also minimizing the civilian use of HEU. The objective of the effort is to aid the development of a reliable, domestic, commercial supply of Mo-99 that avoids a single point of failure and does not require the use of HEU. Towards this effort the GTRI is currently funding exploration into technology pathways for stable production of Mo-99. The pathway we are exploring is production by photon capture in Mo-100 using an electron accelerator and a bremsstrahlung target.

In 2010 we conducted three scaled demonstration experiments to validate designs and processes associated with engineering design support for the commercial accelerator production of Mo-99. These included two low-power production tests with natural Mo and one low-power production test with enriched Mo-100. The MCNPX and CINDER'90 codes were used to support experiment design and for radiation safety planning [1,2]. The radiation transport code MCNPX was used for heating calculations for thermal design inputs, radionuclide production rate and neutron flux calculations for transmutation calculation inputs, and for post irradiation exposure rate calculations. The transmutation code CINDER'90 was used for radionuclide inventory calculations and to generate decay photon spectra used in the post irradiation exposure rate calculations. We studied sensitivity of calculation results to input beam parameters including energy, position, and profile in order to determine beam diagnostic requirements.

By design MCNPX-CINDER'90 radionuclide inventory calculations for accelerator induced radioactivity are performed by first running MCNPX to calculate neutron fluxes and spallation product yields for input to CINDER'90. CINDER'90 is then run for a user-supplied beam history. MCNPX physics models are normally used for the transport of all radiations other than neutrons below 25 MeV because it is the physics models that generate the residual nuclei data stored in the history file used to produce production rate input for CINDER'90. The CINDER'90 library includes only residual production cross-section data for neutron reactions below 25 MeV. For these calculations, rather than using physics models, evaluated photonuclear cross-section data were used to write the tally data cards needed to calculate production rates for CINDER'90 input.

From our calculations we recognized going into the experiments with 6 mm diameter targets that radionuclide yields and post irradiation dose rates would depend strongly on electron beam parameters. In an effort to control beam profile and limit flange heating we used an aluminum collimator with a 6 mm diameter aperture and sufficient length to reduce the calculated ratio of secondary electron emission to primary beam transmission to less than 0.5%. We used beam current monitors upstream and downstream of the collimator and tuned the beam to have downstream current equal to 50% of upstream current. Assuming an aligned Gaussian beam profile, this implies a beam with full-width-half-maximum (FWHM) of 6 mm in both the vertical and horizontal is incident on the collimator. A theodolite was used to physically align the target, collimator and beam line. To actually measure the beam position and profile at the target we placed natural Mo foils in a holder fixed to the target assembly. Post irradiation, Gafchromic film was exposed in contact with the foils. Exposed films were scanned and analyzed to determine FWHMs and offsets. A magnetic spectrum analyzer was used to measure beam energy and energy spread upstream of the collimator.

Post irradiation target doses rates and Mo-99 yields were lower than our calculations predicted assuming an aligned 6 mm FWHM beam incident on the collimator. We saw from the film measurements significantly larger beam spots that were well fit by Gaussian distributions in both the vertical and horizontal. This is evidence of beam divergence in the 30 cm gap between our collimator and target that our MCNPX models did not account for. Rerunning our calculations with the film measured beam profiles we found better code prediction of dose rates and Mo-99 yields, but calculated dose rates remained high. Since ENDF/B-VII photonuclear data does not identify residual nuclei by isomeric state we estimated isomer yields assuming that production is inversely proportional to the difference in spin between the target and the residual states. This method followed an observation that, in general, production of the isomer nearer in spin to that of the target is favored. Looking for Mo-93m, a significant dose contributor in the original calculations for natural Mo targets, in measured gamma spectra suggested we were overestimating its production rate. Revising our isomer yield algorithm, developing on a notional relationship between isomer to ground state yield ratio and spin deficit presented in Ref. 3, we find more reasonable Mo-93m yield prediction and better agreement between calculated and measured target dose rates. In this paper we will present results of our beam parameter sensitivity studies, the methodology used for our post irradiation calculations and compare our calculation results with measured yields and dose rates.

II. EXPERIMENTAL TARGET MODEL

Figure 1 presents plots of the low-power scaled production target model that was prepared from the engineering drawing used to procure target assemblies. It includes seven nominally 3-mm thick, 6-mm-diameter Mo target disks separated by 0.5 mm wide cooling-water channels. The target holder is inserted through a hole in the target housing flange. The front face of the target housing is 0.508 mm (20 mils) thick. The target housing wall is 1.5 mm thick. The walls of the cooling water inlet and outlet are 1 mm thick. The target housing flange and the flange on the back of the target holder are both 7.239 mm thick, with a 33.782 mm diameter. The overall length of the target assembly, less the foil frame, is 55.045 mm. The foil frame, used to hold an activation foil for integrated beam-spot size measurements, is 3.5814 mm thick, with 6.35 mm wide sides holding a 50.8 mm by 50.8 mm (2 in. × 2 in.) Mo foil with a thickness of 0.254 mm (10 mils). The target holder, foil frame, and target housing flange are made of type 304 stainless steel. The target housing wall, front face, and cooling water inlet and outlet are made of Inconel-718.

The natural Mo composition used for the foils and natural target model was based on natural isotopic distributions [4]. We assumed the composition includes impurities as reported in Ref. 5. Laser-ablation, inductively coupled-plasma mass spectrometry (LA-ICP-MS) was used to measure the distribution of Mo isotopes in the Mo-100 enriched material. The results were used to prepare composition input for the model. Impurities with concentrations >10 ppm were included from a manufacturers certificate for the specified material [6]. Impurity elements were assumed present with natural isotopic distributions. The natural material was metallic and the enriched material was sintered. Both had densities of approximately 9.9 g/cm^3. This density was assumed for 6-mm-diameter disks and the model disk thicknesses were calculated to conserve the measured mass of each disk. The calculated disk thicknesses ranged from 2.94 mm to 3.05 mm. The nominal 0.5 mm cooling channel widths were adjusted to accommodate.

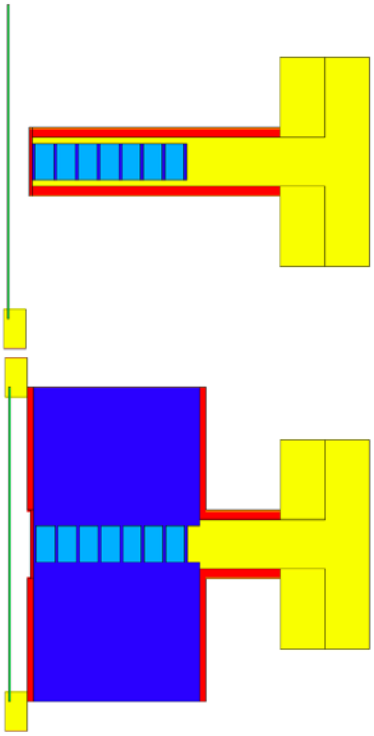

Fig. 1. Low-power scaled-production target model (horizontal section upper, vertical section lower).

III. CALCULATION METHODOLOGY

Electrons were modeled incident on the target model according to measured beam parameters using MCNPX. Photonuclear production rates for residual nuclei were calculated using photon flux tallies multiplied by cross sections provided on de and df cards. Interpreted ENDF data from the ENDF/B-VII.0 library was downloaded from http://www.nndc.bnl.gov for each of the nuclides in the material compositions of the MCNPX models. The Mo material compositions are listed in Table I. Code was written to read the evaluated data and write MCNPX tally data cards. Cross sections at the energies listed in the interpreted ENDF data were used with linear interpolation. The Mo-100(γ,n)Mo-99 cross section data is plotted in Figure 2. One tally is provided for each reaction in each model cell. This results in numerous tallies, about 3000 for these models. MCNPX was compiled with ntalmx set to 1800 for these calculations. Greater ntalmx was beyond machine/compiler constraints meaning two simulations were required for each model to perform all of the tallies. No data was available for P-31, a stainless steel impurity; therefore, its photonuclear reaction residuals were ignored. This is reasonably expected to be of little radiological consequence because its nearest neighbors that may be produced are short-lived P-30 and P-29 and stable isotopes of silicon. Neutron fluxes were also tallied for CINDER'90 input with the photonuclear production rates.

TABLE I. Mo Material Compositions

Natural Material	
Nuclide	atom%
Na-23	3.40E-03
Fe-54	8.71E-04
Fe-56	1.37E-02
Fe-57	3.16E-04
Fe-58	4.20E-05
Zn-64	1.70E-03
Zn-66	9.76E-04
Zn-67	1.43E-04
Zn-68	6.56E-04
Zn-70	2.17E-05
Zr-90	4.42E-03
Zr-91	9.65E-04
Zr-92	1.47E-03
Zr-94	1.49E-03
Zr-96	2.41E-04
Mo-92	1.48E+01
Mo-94	9.25E+00
Mo-95	1.59E+01
Mo-96	1.67E+01
Mo-97	9.55E+00
Mo-98	2.41E+01
Mo-100	9.63E+00

Enriched Material	
Nuclide	atom%
Si-28	1.97E-02
Si-29	9.99E-04
Si-30	6.59E-04
Al-27	1.11E-02
Fe-54	3.14E-04
Fe-56	4.92E-03
Fe-57	1.14E-04
Fe-58	1.51E-05
Mo-92	3.10E-02
Mo-94	2.20E-02
Mo-95	3.70E-02
Mo-96	4.50E-02
Mo-97	3.90E-02
Mo-98	4.62E-01
Mo-100	9.93E+01
W-180	4.56E-06
W-182	1.01E-03
W-183	5.44E-04
W-184	1.16E-03
W-186	1.08E-03

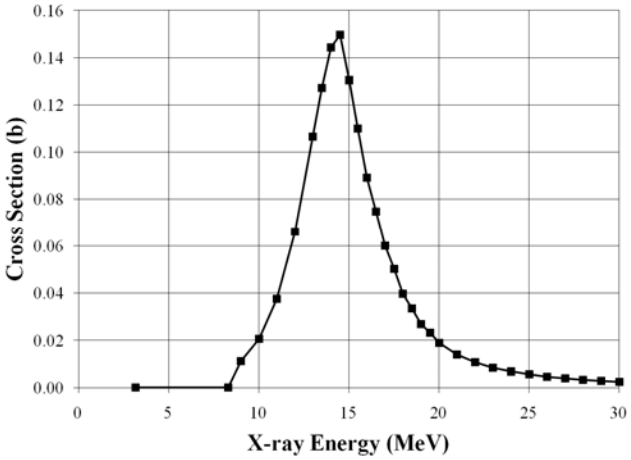

Fig. 2. Mo-100(γ,n)Mo-99 cross section. Points are at energies listed in the interpreted ENDF data.

The MCNPX transport calculations were run with default physics options except that photonuclear particle production was turned on and less than analog production of electron-induced x-rays, knock-on electrons and photon induced secondary electrons was sampled for computational efficiency since it is bremsstrahlung x-rays from beam electrons that dominate yields. By default bremsstrahlung photon production is analog. We ran preliminary calculations to verify that default estep values for our materials were sufficient. Increasing estep for a material increases number of electron sub-steps per energy step, increasing accuracy with a run-time expense.

Code was written to read MCNPX output files and prepare CINDER'90 input files. These include a fluxes file which has the tallied neutron fluxes by cell and a splprod file for each cell that has the tallied residual production rates for the photonuclear reactions. This code splits the production rates for residual nuclei with ground and isomeric states according to spin based approximations for isomer to ground state yield ratios. Before the experiment an algorithm was coded assuming that production is inversely proportional to the difference in spin between the target and the residual states following an observation that production of the state nearer in spin to that of the target is favored. Radiation surveys following the natural target experiments found dose rates much lower than predicted by the pre-experiment calculations. Differences in beam parameters resulted in less activation accounting for much of the difference but the isomer yield approximation was suspected as being another cause. For example, with its 6.9 h half-life, Mo-93m was a significant contributor to the natural molybdenum target dose rates after few hours of cool down. The algorithm used to calculate the isomer yields predicted an isomer to ground yield ratio of $Y_{i.s.}/Y_{g.s} = 0.23$. Few measurements of this ratio exist for photonuclear high spin deficit isomer production reactions as is the case for Mo-94(γ,n)Mo-93m with $\Delta J = -9.5$, where for target spin J_t and isomer spin $J_{i.s.}$, ΔJ is defined as $\Delta J = J_t + 1 - J_{i.s.}$. Two that do exist suggest much lower ratios, Hf-178(γ,p)Lu-177m, $\Delta J = -10.5$, at 0.005 and Au-197(γ,n)Au-196m, $\Delta J = -9.5$, at 0.0005 [3,7].

Ref. 3 presents a notional relationship between ΔJ and the yield ratio of approximately $0.4 \cdot \exp(0.7 \cdot \Delta J)$ based on only 11 reactions. It predicts for $\Delta J = -9.5$, $Y_{i.s.}/Y_{g.s} = 0.0005$. As suggested in Ref. 3 more measurements were considered to further evaluate the notion. Table II lists 49 reactions with measured ratios. $Y_{i.s.}/Y_{g.s}$ are plotted versus ΔJ in Figure 3. The data is highly scattered. A fit to it is $0.62 \cdot \exp(0.34 \cdot \Delta J)$. More than 90% of the measurements fall within an order of magnitude of this fit and about half fall within a factor of two of it. This performance is comparable to MCNPX physics model residual production rate predictions for proton beam transmutation calculations. The fit estimates $Y_{i.s.}/Y_{g.s} = 0.024$ for $\Delta J = -9.5$. This is an order of magnitude lower than initial algorithm predicted for the pre-experiment calculations and two orders of magnitude higher than Ref. 3 suggests.

To independently assess the fit for Mo photonuclear reactions we irradiated a 1-mil thick natural Mo foil with the bremsstrahlung spectrum from a microtron operated at 20 MeV. Using gamma spectroscopy we were able to detect Nb-95, Nb-95m, Mo-99 and Mo-93m. Nb-95 and Nb-95m are produced from Mo-96(γ,p) and Mo-97(γ,np). The energy integrated product of cross sections and bremsstrahlung spectrum indicate that Mo-96(γ,p) accounts for 99.97% of the yield in natural Mo. $\Delta J = 0.5$ for the Mo-96(γ,p)Nb-95m reaction and calculated from our measured activities $Y_{i.s.}/Y_{g.s} = 2.13 \pm 0.04$ for Mo-96(γ,p). In natural Mo, Mo-93 and Mo-93m are produced from Mo-94(γ,n), 95.63%, and Mo-94(γ,2n), 4.37%. Mo-93 ground state has a very long half-life, 3500 years, and decays by electron capture with associated very low energy x-rays and was not detectable. Based on cross sections and bremsstrahlung spectrum the total production rate of Mo-93, ground and isomer, is 94.5% of the Mo-99 production rate in natural Mo. Using this to estimate the total Mo-93 production rate from the measured Mo-99 activity we calculate from our measured Mo-93m activity that $Y_{i.s.}/Y_{g.s} = 0.00188 \pm 0.00002$ for the Mo-94(γ,n) reaction, ignoring contribution from Mo-94(γ,2n). We also did not correct for contributions from Mo-92(n,γ) or Mo-98(n,γ). From our calculations these are < 0.5%. The errors on our yield ratios only include counting errors. Systematically they are certainly higher. Our measurements are plotted in Figure 3 for comparison with fit to referenced measurements. The ratios of the fit to the measurements are 13 and 0.35, for Mo-94(γ,n) and Mo-96(γ,p) respectively.

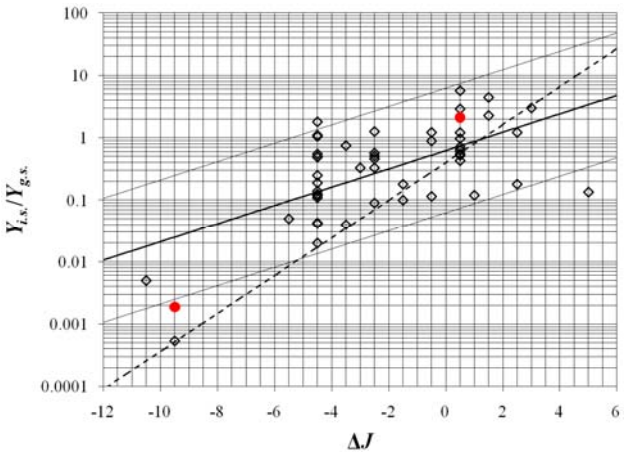

Fig. 3. Isomeric to ground state yield ratios of Table II reactions plotted versus ΔJ. Heavy solid line is fit to reaction data points. Thin solid lines are 10 times and 0.1 times fit. Heavy dashed line is notional line from Ref. 3. Solid red circles are our measurements for Mo-94(γ,n), $\Delta J = -9.5$, and Mo-96(γ,p), $\Delta J = 0.5$.

TABLE II. Spin and Isomeric to Ground State Yield Ratio Measurement Data for Photonuclear Reactions

Target	Reaction	Isomer	J_t	$J_{g.s.}$	$J_{i.s.}$	$Y_{i.s.}/Y_{g.s}$	ΔJ	Ref.
Hf-178	γ,p	Lu-177m	0	3.5	11.5	0.005	-10.5	3
Au-197	γ,n	Au-196m	1.5	2	12	0.00054	-9.5	7
Hg-198	γ,n	Hg-197	0	0.5	6.5	0.05	-5.5	8
Nd-142	γ,n	Nd-141m	0	1.5	5.5	0.043	-4.5	7
Sm-144	γ,n	Sm-143m	0	1.5	5.5	0.042	-4.5	3
Re-185	γ,n	Re-184m	2.5	3	8	0.02	-4.5	3
Ag-107	γ,n	Ag-106m	0.5	1	6	0.55	-4.5	8
Pd-108	γ,n	Pd-107m	0	2.5	5.5	0.5	-4.5	8
Pd-110	γ,n	Pd-109m	0	2.5	5.5	0.11	-4.5	8
Cd-116	γ,n	Cd-115m	0	1	5.5	0.25	-4.5	8
Ce-140	γ,n	Ce-139m	0	1.5	5.5	0.14	-4.5	8
Ce-140	γ,3n	Ce-137m	0	1.5	5.5	1.1	-4.5	8
Nd-144	γ,3n	Nd-141m	0	1.5	5.5	1.8	-4.5	8
Ba-138	γ,n	Ba-137m	0	1.5	5.5	0.12	-4.5	9
Te-120	γ,n	Te-119m	0	0.5	5.5	1.05	-4.5	7
Te-130	γ,n	Te-129m	0	1.5	5.5	0.49	-4.5	7
Ce-138	γ,n	Ce-137m	0	1.5	5.5	0.13	-4.5	7
Ce-140	γ,n	Ce-139m	0	1.5	5.5	0.19	-4.5	7
Ta-181	γ,p	Hf-180m	3.5	0	8	0.04	-3.5	3
Hf-179	γ,p	Lu-178m	4.5	1	9	0.75	-3.5	3
Y-89	γ,2n	Y-87m	0.5	0.5	4.5	0.33	-3	7
Ta-180m	γ,p	Hf-179m2	9	4.5	12.5	0.09	-2.5	3
Ge-76	γ,n	Ge-75m	0	0.5	3.5	1.26	-2.5	7
Br-81	γ,n	Br-80m	1.5	1	5	0.46	-2.5	7
Se-82	γ,n	Se-81m	0	0.5	3.5	0.57	-2.5	7
Rb-85	γ,n	Rb-84m	2.5	2	6	0.33	-2.5	7
Ta-181	γ,3n	Ta-178m	3.5	1	7	0.51	-2.5	8
Lu-175	γ,n	Lu-174m	3.5	1	6	0.1	-1.5	3
Sc-45	γ,n	Sc-44m	3.5	2	6	0.18	-1.5	7
Cl-35	γ,n	Cl-34m	1.5	0	3	0.89	-0.5	8
Co-59	γ,n	Co-58m	3.5	2	5	1.22	-0.5	7
Se-74	γ,n	Se-73m	0	4.5	1.5	0.115	-0.5	10
Sr-86	γ,n	Sr-85m	0	4.5	0.5	0.64	0.5	7
Zr-90	γ.n	Zr-89m	0	4.5	0.5	1.21	0.5	7
Mo-92	γ,n	Mo-91m	0	4.5	0.5	0.97	0.5	8
In-115	γ,n	In-114m	4.5	1	5	5.67	0.5	8
Mo-94	γ,3n	Mo-91m	0	4.5	0.5	0.63	0.5	8
Mo-98	γ,p	Nb-97m	0	4.5	0.5	0.71	0.5	10
Sn-112	γ,p	In-111m	0	4.5	0.5	0.43	0.5	7
Sn-118	γ,p	In-117m	0	4.5	0.5	2.9	0.5	7
Mo-96	γ,p	Nb-95m	0	4.5	0.5	0.555	0.5	7
Mo-98	γ,p	Nb-97m	0	4.5	0.5	0.52	0.5	7
Hf-178m2	γ,n	Hf-177m2	16	3.5	16	0.12	1	3
In-113	γ,n	In-112m	4.5	1	4	4.43	1.5	7
Mn-55	γ,3n	Mn-52m	2.5	6	2	2.27	1.5	8
K-39	γ,n	K-38m	1.5	3	0	1.22	2.5	8
Ti-47	γ,p	Sc-46m	2.5	4	1	0.18	2.5	7
Ta-180m	γ,2n	Ta-178m	9	1	7	3	3	3
In-113	γ,2n	In-111m	4.5	4.5	0.5	0.135	5	7

Calculations after the experiments were run with measured beam parameters and code preparing CINDER'90 inputs that used the fit to Table II data for isomer yields. Measured beam profile, position and energy data was used to prepare source data cards for MCNPX. CINDER'90 was run for each model cell using measured average beam current and irradiation time for beam history input with post irradiation decay time steps out to one month. The gamma_source script distributed with CINDER'90 was used to generate source data cards that were then used for post irradiation dose rate calculations with MCNPX.

IV. BEAM PARAMETER SENSITVITY

Prior to the experiments beam parameter sensitivity was studied to develop requirements for diagnostics. These studies also provide information that can be used to bound systematic uncertainty in calculated yields. Beam was modeled incident on the collimator. Vertical and horizontal FWHM, assumed equal, was varied about the planned 6-mm dimension and alignment sensitivity was evaluated by varying beam position and moving the collimator out of alignment. Alone ±2-mm variations in FWHM affect total Mo-99 yield by a factor of 1.7.

Figure 4 illustrates sensitivity to beam size and alignment. The target and collimator are assumed to be aligned and the beam is offset. For > 6-mm FWHM, < 1-mm beam offset results in < 5% yield reduction. For larger beam spots Mo-99 yield is less sensitive to beam position but less of the beam gets to target resulting in lower yields. Figure 5 illustrates sensitivity to collimator alignment with the target. The beam is assumed to be aligned with the target but the collimator is offset. Yield is more sensitive to collimator-target alignment than beam alignment. For > 6-mm FWHM, 1-mm collimator offset results in > 10% yield reduction. Impact of misalignment is more significant for larger spot sizes. Figure 6 illustrates sensitivity to beam energy. At 6-mm FWHM, < 1% energy offset has < 5% yield impact.

A magnetic spectrum analyzer expected to measure mean beam energy to within 0.1% was used to measure the energy spectrum of the beam prior to each experiment. To minimize alignment uncertainty a theodolite was used to align the target housing and collimator with the beam pipe. The estimated tolerance for the alignment procedure is 0.1 mm. For beam position and profile measurements we investigated use of a wire beam position monitor (WBPM), a yttrium aluminum garnet (YAG) screen, an optical transition radiation (OTR) system, and activation foils. All of the options have one or more performance or operational limitations. We have recently installed and tested an OTR system but for the 2010 experiments we were limited to using activation foils, measuring beam position and profile at the target.

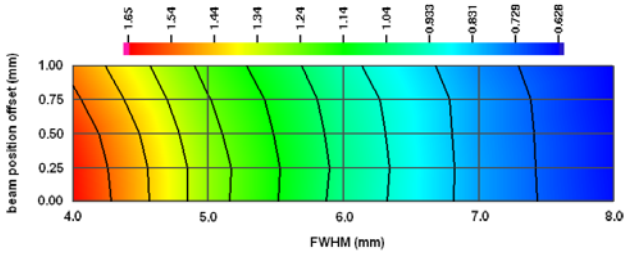

Fig. 4. Mo-99 yield sensitivity to beam size and position (normalized to 6 mm FWHM with no offset).

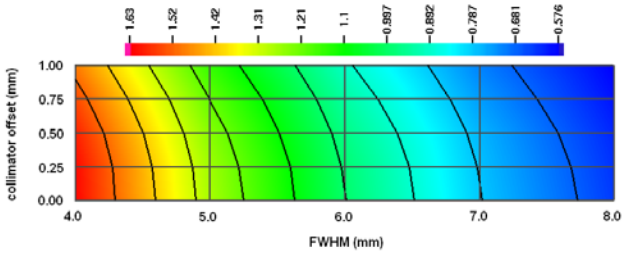

Fig. 5. Mo-99 yield sensitivity to beam size and collimator alignment (normalized to 6 mm FWHM with no offset).

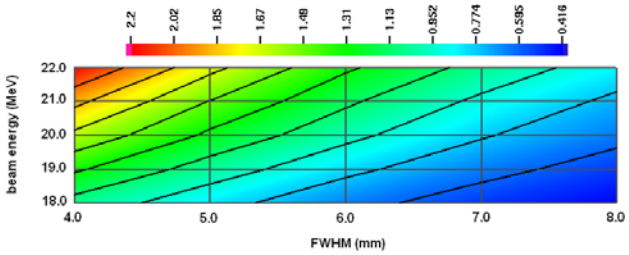

Fig. 6. Mo-99 yield sensitivity to beam size and energy (normalized to 6 mm FWHM at 20 MeV).

10-mil thick natural Mo foils were in place in front of the target during each irradiation. Gafchromic films were exposed in contact with the activation foils after the irradiations. Exposed films were scanned and analyzed to determine position and profile. Because secondary photons are activating the foil rather than the primary beam, and the film exposure is to a spatially distributed isotropic source, a systematic error is introduced to the profile measurement and the handling required introduces position uncertainty. An MCNPX-CINDER'90 simulation of the process is illustrated in Figure 7. A 20 MeV electron beam with 6-mm FWHM was modeled incident on the foil in the holder upstream of the target and tallies of electron beam current and subsequent film exposure were made in 1 mm wide rings about the beam centerline. A broadening of the profile is evident. Figure 8 provides an example of film analysis. Our Gaussian fits were made in regions about the peak ignoring the background tails. From simulation we estimate the systematic error for the profile measurement to be about a 0.2-mm overestimate for a 6-mm FWHM, and in general about 5%.

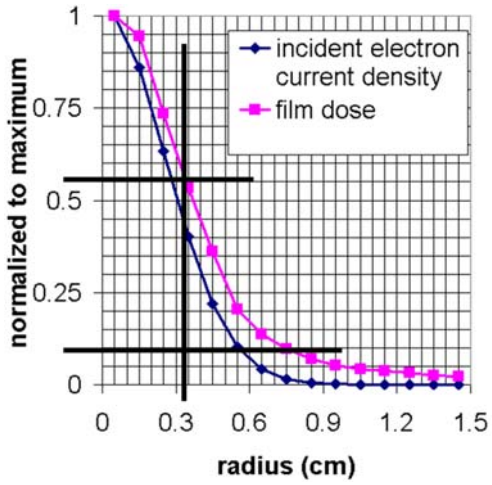

Fig. 7. Simulation of foil-film measurement of beam profile. Lines illustrate FWHM estimate from film ignoring background tail.

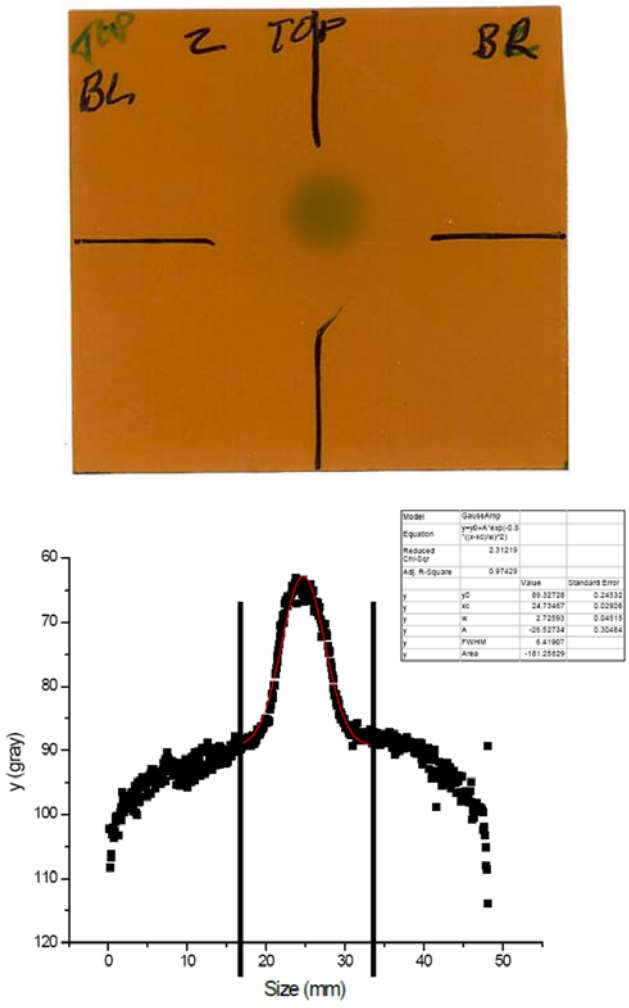

Fig. 8. Scanned film (top) and subsequent gray scale beam profile analysis (bottom).

V. CALCULATIONS AND MEASUREMENTS

The measured beam parameters for the three experiments used for calculations are listed in Table III. The beam sizes and offsets were unexpected considering the collimator and indicate an angular distribution or skew not measured or modeled. Steering the beam through the collimator was difficult and the foil-film profiles suggest beam may have been divergent and not parallel with the target axis. For the calculations the beam current, size and position at the target were assumed without simulation of transport through the collimator. The beam was assumed to be parallel to the axis. The tabulated beam energies are averages. The energy FWHMs were approximately 0.4 MeV. The average energies were assumed for the calculations. We do not expect this introduced significant error based on our sensitivity studies.

TABLE III. Measured Beam Parameters

Parameter	Natural 1	Natural 2	Enriched
Beam Energy	19.9 MeV	20.1 MeV	20.2 MeV
Current to Collimator	82 μA	80 μA	80 μA
Current to Target	40 μA	40 μA	45 μA
X FWHM at Target	9.0 mm	6.4 mm	7.0 mm
Y FWHM at Target	9.0 mm	8.0 mm	7.2 mm
X Offset at Target	1.1 mm	0.6 mm	-1.2 mm
Y Offset at Target	0.0 mm	3.0 mm	-0.7 mm
Irradiation Time	20 min	27 min	82 min

Tables IV, V and VI list calculated and measured end-of-bombardment (EOB) Mo-99 activities by target disk for the three experiments. Measurements were by gamma spectroscopy with self shielding correction and decay correction back to time irradiation ended. Calculations were run using both the normal MCNP style bin-centered energy indexing treatment and the Integrated Tiger Series (ITS) style nearest group boundary treatment available as a debug option in MCNPX. The medical physics community has shown that dose depth curve calculations for electron beams are improved using ITS treatment [11]. Total activity agreement appears remarkable using either treatment for the natural target experiments. The overestimate for the enriched target could be due to poor position and profile measurement. Calculations before the experiments overestimated total Mo-99 activities by about 50% assuming measured beam currents at collimator with 20 MeV, 6-mm FWHM beam.

TABLE IV. EOB Mo-99 Activities – Natural Target 1

Disk	Activity (μCi)			Difference	
	Measured	MCNP	ITS	MCNP	ITS
1	57.6	50.8	50.2	-12%	-13%
2	53.6	55.3	53.3	3%	-1%
3	37.6	39.5	38.0	5%	1%
4	28.3	29.6	28.3	5%	0%
5	19.6	22.4	21.4	14%	9%
6	14.6	17.1	16.3	17%	12%
7	11.0	13.4	12.8	22%	17%
Total	222	228	220	3%	-1%

TABLE V. EOB Mo-99 Activities – Natural Target 2

Disk	Activity (μCi)			Difference	
	Measured	MCNP	ITS	MCNP	ITS
1	95.2	74.4	73.3	-22%	-23%
2	85.9	82.1	79.1	-4%	-8%
3	58.2	59.9	57.2	3%	-2%
4	36.4	43.2	40.8	18%	12%
5	29.4	32.8	31.0	11%	5%
6	21.7	25.5	24.0	17%	11%
7	15.3	20.7	19.5	35%	28%
Total	342	339	325	-1%	-5%

TABLE VI. EOB Mo Mo-99 Activities – Enriched Target

Disk	Activity (mCi)			Difference	
	Measured	MCNP	ITS	MCNP	ITS
1	2.93	3.18	3.15	9%	8%
2	2.84	3.55	3.45	25%	21%
3	1.95	2.53	2.45	30%	26%
4	1.33	1.82	1.76	37%	32%
5	0.99	1.35	1.31	36%	32%
6	0.69	1.02	0.99	48%	44%
7	0.53	0.79	0.77	49%	44%
Total	11.3	14.2	13.9	26%	23%

The pre-experiment calculation discrepancy appears largely explained by beam parameters. The increasing trend in differences going from front to back we believe most likely is a result of divergent or not normally incident beam. Overestimates at depth are lower using the ITS energy indexing treatment. This is consistent with the medical physics dose depth curve calculation results. The differences with depth are plotted for comparison in Figure 9.

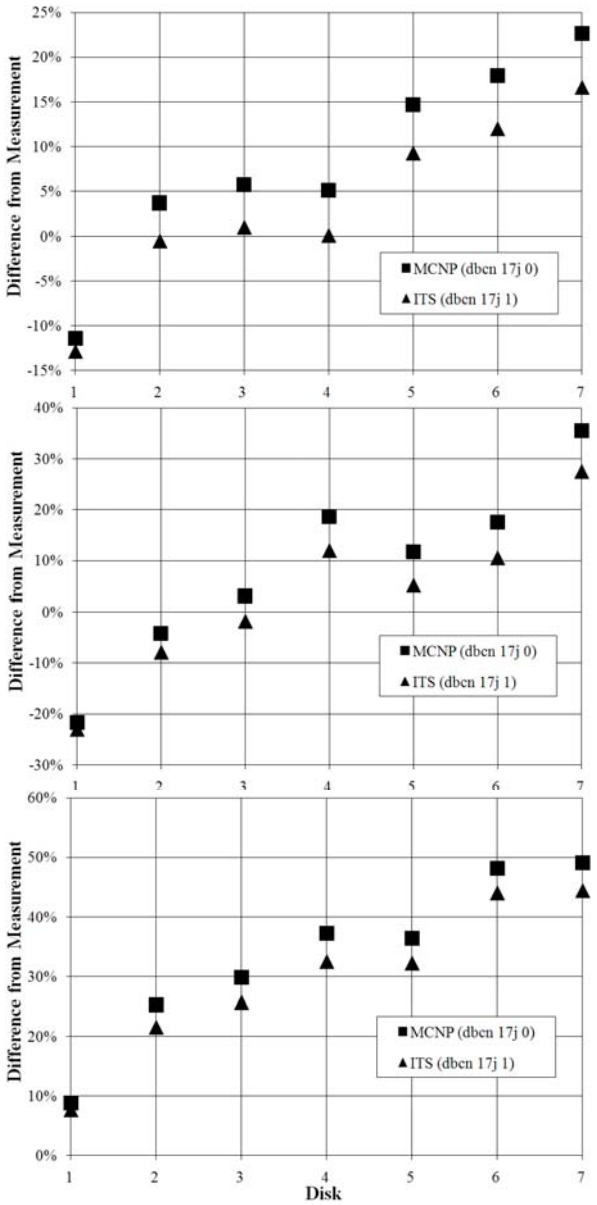

Fig. 9. Mo-99 activity differences between calculation and measurements by disk for MCNP and ITS style energy indexing (top – natural 1, center – natural 2, bottom – enriched).

Exposure rate calculations were run using the decay photon spectra generated by CINDER'90 and formatted for MCNPX input using the gamma_source script. The target holders with activated disks were surveyed upon removal from the target housing. Table VII compares calculation and survey results. Calculations agree with survey results to within a factor of two for all three experiments. The decay gamma spectra are based on all radioactive products of the transmutation calculations. Table VIII lists products at EOB with activities > 1 μCi from the calculations performed with ITS style energy indexing.

TABLE VII. Target Exposure Rates

Target	Minutes after EOB	30 cm Exposure Rate (mR/h)			Ratio	
		Survey	MCNP	ITS	MCNP	ITS
Natural 1	1195	1.5	0.74	0.72	0.50	0.48
Natural 2	165	3.0	2.3	2.2	0.75	0.72
Enriched	160	22	26	26	1.18	1.16

TABLE VIII. Target Disk EOB Activities > 1 μCi

Nuclide	Half-Life (s)	EOB Activity (μCi)		
		Natural 1	Natural 2	Enriched
Al-26m1	6.35E+0			1.02E+0
Zr-89m1	2.51E+2	6.39E+0	7.34E+0	
Zr-90m1	8.09E-1	9.48E+2	1.05E+3	3.40E+0
Zr-91m1	4.35E-6	7.97E+1	8.78E+1	
Nb-91m1	5.36E+6	2.70E+0	4.03E+0	
Nb-91m2	3.60E-6	1.74E+4	1.92E+4	5.56E+1
Nb-94m1	3.76E+2	5.13E+2	6.25E+2	2.19E+0
Nb-95m1	3.12E+5	1.38E+0	2.14E+0	
Nb-96	8.41E+4	2.18E+0	3.42E+0	
Nb-97	4.33E+3	2.95E+1	4.58E+1	3.10E+0
Nb-97m1	6.00E+1	7.36E+1	8.66E+1	2.43E+0
Nb-99	1.50E+1	1.02E+1	1.25E+1	1.92E+2
Nb-99m1	1.56E+2	7.48E+0	9.16E+0	1.41E+2
Mo-91	9.29E+2	1.76E+4	2.37E+4	9.78E+1
Mo-91m1	6.52E+1	1.62E+4	1.83E+4	5.39E+1
Mo-93m1	2.50E+4	4.07E+1	6.09E+1	
Mo-99	2.37E+5	2.20E+2	3.25E+2	1.39E+4
Mo-101	8.77E+2			2.56E+3
Tc-99m1	2.16E+4	3.68E+0	7.30E+0	9.16E+2
Tc-101	8.53E+2			2.22E+3
W-183m1	5.20E+0			5.35E+0
W-185m1	1.00E+2			3.04E+0

VI. CONCLUSIONS

The MCNPX-CINDER'90 calculations run after the experiments using measured beam parameters reproduced measured Mo-99 activities and exposure rates reasonably well. Activity discrepancies are most likely due to beam divergence and skew and errors in the beam position measurements that were made using activation foils with subsequent film exposures. The energy indexing treatment used for electron transport calculations has a notable effect on results. With ITS style treatment calculated activities are lower and the distribution with depth is more toward the front of the target. Though from our experiments it is difficult to judge which treatment is better it appears the ITS style is. It reduces the discrepancy trend with depth that we expect is mostly a result of beam angular distribution and alignment.

Exposure rates calculated using measured beam parameters and our revised algorithm for estimating isomer to ground state yield ratios reproduces post irradiation survey results to within a factor of two. We are likely at the limits of what a spin based approximation of the ratios can do. For future calculations we will use measured yield ratios where available.

We are planning foil activation studies without collimation of the electron beam that will be less sensitive to beam alignment. We are also developing better beam diagnostics for future experiments. In these we plan to study more of the expected reactions that could be significant to the development of a production facility.

ACKNOWLEDGMENTS

We acknowledge the National Nuclear Security Administration's Global Threat Reduction Initiative (NA 21) for sponsorship of this work. We acknowledge Los Alamos National Laboratory's Non-Destructive Testing & Evaluation group (AET-6) for supporting our isomer to ground state yield ratio measurements.

REFERENCES

1. D.B. Pelowitz, ed., "MCNPX™ User's Manual," Los Alamos National Laboratory report LA-CP-07-1473 (April 2008).
2. W.B. Wilson, S.T. Cowell, T.R. England, A.C. Hayes, P. Moller, "A Manual for CINDER'90 Version 07.4 Codes and Data," Los Alamos National Laboratory report LA-UR-07-8412, Version 07.4.2 Update (March 2008).
3. S.A. Karamian, J. de Doer, Yu.Ts. Oganessian, A.G. Belov, Z. Szeglowski, B.N. Markov, J. Adam, V.I. Stegailov, Ch. Briancon, O. Constantinescu, M. Hussonnis, "Observation of photonuclear reactions on isomeric targets: $^{178}Hf^{m2}(\gamma,n)^{177}Hf^{m2}$, $^{180}Ta^{m}(\gamma,n)^{178}Ta^{m,g}$ and $180Ta^{m}(\gamma,p)^{179}Hf^{m2}$," *Z. Phys. A* **356**, 23–29 (1996).
4. E.M. Baum, H.D. Knox, T.R. Miller, et al., *Nuclides and Isotopes*, 16th edition, Knolls Atomic Power Laboratory, Inc., Schenectady, New York (2002).
5. K.S. Park, N.B. Kim, Y.S. Kim, K.Y. Lee, H.W. Choi, Y.Y. Yoon, "Determination of U, Th and Other Impurities in Molybdenum by Radiochemical Neutron Activation Analysis," *J. Rad. Nuc. Chem.* **123**:2, 585–592 (1988).
6. ISOFLEX USA, Certificate of Analysis No. 42-01-100-1288 (October 1, 2009).

7. S.R. Palvanov, O. Razhabov, “Isomer Yield Ratios of Photonuclear Reactions at $E_{\gamma max}$ 25 and 30 MeV,” *Atomic Energy* **87**:1, 533–536 (1999).
8. H. Bartsch, W. Geunther, K. Huber, U. Kneissl, H. Krieger, “Systematic Trends in Analysis of Photonuclear Cross Section Ratios,” *Z. Phys. A* **285**, 71–75 (1978).
9. N. Tsoneva, C. Stoyanov, Y.P. Gangrsky, V.Y. Ponomarev, N.P. Balabanov, A.P. Tonchev, “Population of Isomers in the Decay of Giant Dipole Resonance,” *Phys. Rev. C* **61**, 044303 (2000).
10. M.G. Davydov, V.G. Magera, A.V. Turkhov, E.M. Shomurodov, “Isomeric Ratios of the Yields of Photonuclear Reactions for Gamma Activation Analysis,” *Atomic Energy* **58**:1, 47-50 (1985).
11. H.A. Neddaie, M.A. Modleh-Shirazi, H. Gharaati, M. Shariari, M. Allahverdi, “Assessment of Different MCNP Monte Carlo Codes in Electron Absorbed Dose,” *Rep. Pract. Oncol. Radiother.* **11**:6, 293-298 (2006).